Supplementary Material

Crystal plasticity of nanotwinned microstructures: A discrete twin approach for copper

HamidReza Mirkhani and Shailendra P. Joshi

S1. Apparent Macroscopic Hardening in Microstructures with Non-Hardening Slip Systems:

In Fig. 6, the regimes I and II of the green curve that is dominated by the nucleation driven slip (first term on the rhs of Eq. 10a), show a hardening behavior at small strains beyond the incipient yield (first blue circle). This seems surprising at first as the nucleation term does not evolve with a hardening rule. Consequently, at least up to this stage of deformation the hardening in Fig. 6 cannot be attributed to the hardening in g^{α}. Therefore, we ask: what is the underlying mechanics behind the macroscopic hardening in the initial stress-strain response of an nt-structure even when the underlying plasticity law is non-hardening type? The possible ingredients that determine this behavior are: (i) the Schmid factors of the twinned orientations, (ii) IRSS on the β slip systems, and (iii) applied displacement (Δu) constraints on the grain edges. To investigate the roles of these effects on the apparent macroscopic hardening, we set up the following models:

- a bi-lamellar model with twin orientation ($\theta = 24.7^{\circ}$) (Fig. S1-a), and
- two (corresponding to the two twin variants) *twin-free* single crystal models for comparison. We call them variants V_1 and V_2.

In all the cases the slip system strengths is assumed to be of non-hardening type. To understand the role of IRSS we simulate each model with $\bar{\tau}_b^{\beta} = 0{,}50$ and $200MPa$. Finally, to investigate the effects of the b.c's, we consider the twin-free models with and without b.c.'s at the top and bottom edges keeping the b.c's at the left and right edges unchanged.

Figure S1-b shows a comparison of the hardening responses between the incipient yield and the profuse yielding beyond which the macroscopic response degenerates to a perfectly plastic behavior. The most interesting result is that the initial hardening after the first yield seems to be a ubiquitous phenomenon that is determined by the level of anisotropy between the CRSS of the α and β slip

systems rather than the Schmid factor (i.e. irrespective of whether it is a single crystal or a twinned microstructure). This anisotropy is induced by the level of $\bar{\tau}_b^{\beta}$ on the β slip systems and for $\bar{\tau}_b^{\beta} = 0$ the incipient yield is the macroscopic yield as in the case perfect plasticity that is dominated by single slip. Secondly, a bi-lamellar response is an average of their single crystal variants for all the values of $\bar{\tau}_b^{\beta}$. This is logical because the given θ the one of the single crystal variants has a lower Schmid factor than the other.

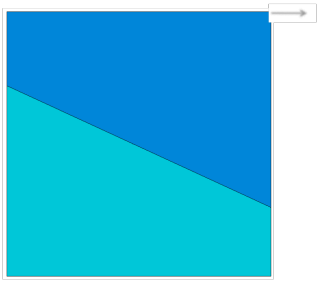

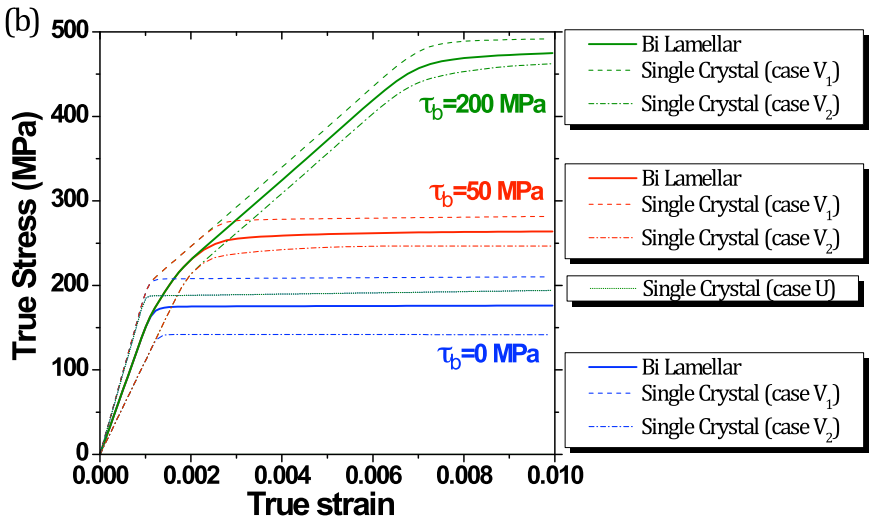

Figure S1- (a) A bi-lamellar *twinned* grain ($\theta = 24.7^{\circ}$) with non-hardening slip systems, (b) the macroscopic stress-strain responses for the bi-lamellar model (solid lines), twin-free single crystal variants suppressing (dashed and dashed-dotted lines), and allowing (short dotted line) tensile axis rotation.

Having understood that it is the CRSS anisotropy rather than Schmid factor that induces hardening, the next question is to ask as to why this is so. The answer to this lies in the nature of edge constraints. It turns out that the reason the hardening is observed is because the enforced b.c.'s at the top and bottom edges of the models (Fig. S1-a) suppress the tensile axis rotation of the grain. Because of the constraint, the lattice has to rotate instead and this brings the β slip systems that are strengthened by internal stress

into action. This is most easily demonstrated by the simulations for the V_1 case, but with no constraints on the top and bottom edges (Fig. S1-b, Case U). Note that irrespective of whether $\bar{\tau}_b^{\beta}$ is present or not, the response is identical, clearly underscoring the significance of the constraints. The same mechanism is expected to prevail within the grains of an nt-polycrystal even if all the slip systems were to be of non-hardening type. In real microstructures the constraints felt by the grain boundaries from the neighboring is expected to be in between these two extreme cases and consequently, the level of induced hardening will be modulated.

S2. Contour Plots of Total Plastic Slip in Single-Grain with $\theta = 24.7^{\circ}$ and $\lambda = 15nm$.

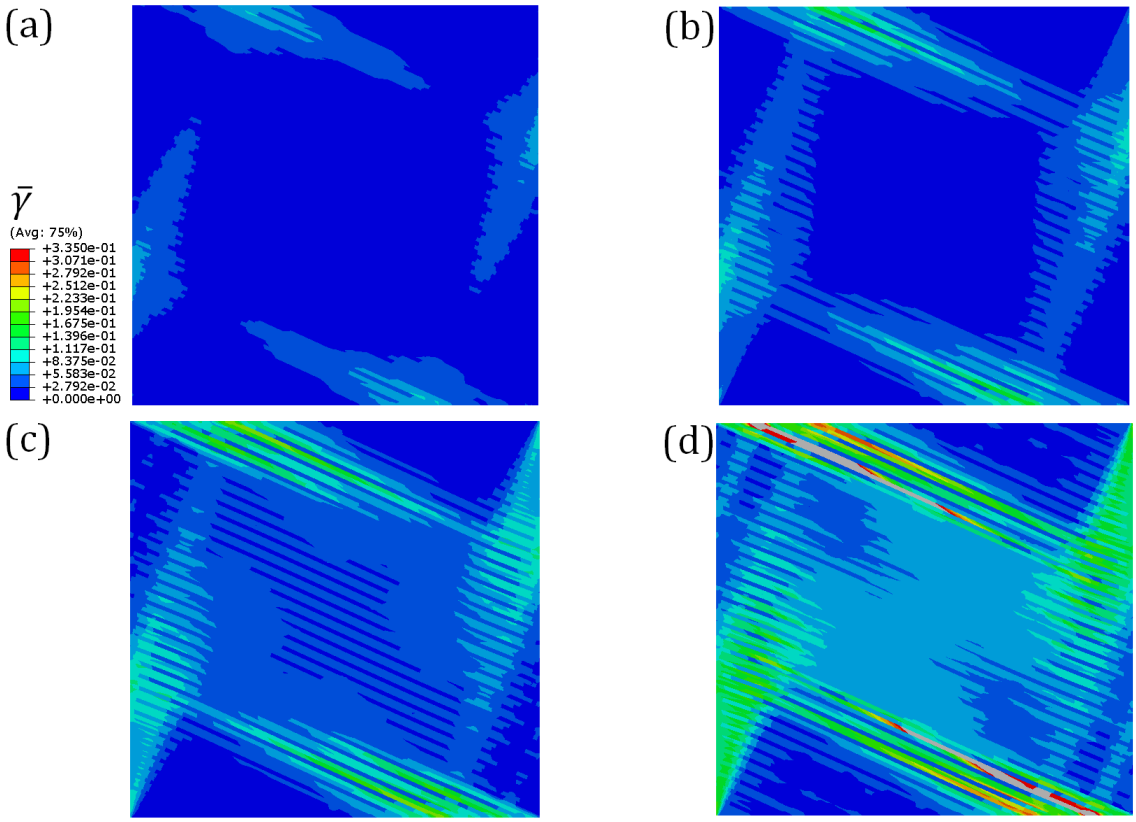

Figure S2. The contour of cumulative plastic slip $\bar{\gamma}$ for the single grain with $\theta = 24.7^{\circ}$ and $\lambda = 15nm$ at (a) $\bar{\varepsilon} = 0.01$, (b) $\bar{\varepsilon} = 0.015$, (c) $\bar{\varepsilon} = 0.02$, and (d) $\bar{\varepsilon} = 0.03$. Similar to the case of the single grain with $\theta = 54.7^{\circ}$, as deformation progresses, plastic slip starts to localize at the boundary zones as a result of resistance to tensile axis rotation.

S3. Computational Expense:

Here we provide some information regarding used model, such as number of elements, nodes, and job-running times. In single grain models, we consider four orientations, $\theta = 54.7^{\circ}, 24.7^{\circ}, 9,7^{\circ}, 0^{\circ}$, and for each orientation we consider six TB spacing, $\lambda = 100, 40, 15, 10, 8, 4nm$, totally 24 models. As FE specifications of these models are almost in the same order, we provide FE specifications of the models with only $\lambda = 15nm$ in Table S1.

Table S1 – FE model specifications of some single-grains with $\lambda = 15nm$ up to 3% true strain					
è	**No. of Nodes**	**No. of Elements**	**Job-Running Time**	**No. of CPUs**	**Max. Step Size (Sec.)**
24.7°	76,419	151,774	$3H:30'$	2	0.05
0°	57,058	57,485	$3H:30'$	2	0.05

FE specifications of the polycrystals with 6×6 matrix of single grains are also presented in Table S2.

Table S2 – FE model specifications of some polycrystals, up to 2% true strain					
ë(nm)	**No. of Nodes**	**No. of Elements**	**Job-Running Time (Hours)**	**No. of CPUs**	**Max. Step Size (Sec.)**
40	454,177	904,667	24	4	0.05
15	611,320	1,213,507	52	4	0.01
10	601,914	1,195,871	48	2	0.05

S4. UMAT Implementation of Crystallographic Constitutive Laws for DT-CP:

The computational implementation of the crystal plasticity formulation follows the work of Needleman et al [1] that is modified to include the constitutive expressions outlined in section 3. We provide an outline for the time integration of the plastic slip on i^{th} slip system in the TBAZ region. The

subscript z is omitted for clarity. The final expressions are formally written at the end. The incremental plastic slip $\Delta\gamma^i$ on i^{th} slip system at time increment Δt is

$$\ddot{A}\gamma^i = \gamma^i\left(t + \ddot{A}t\right) - \gamma^i\left(t\right) \tag{S1}$$

Noting that $\dot{\gamma}^i \approx \Delta\gamma^i / \Delta t$ and employing a linear interpolation within Δt, we obtain

$$\ddot{A}\gamma^i = \ddot{A}t\left[\left(1-\zeta\right)\dot{\gamma}_t^i + \zeta\dot{\gamma}_{t+\ddot{A}t}^i\right] \tag{S2}$$

where $\zeta = 0.5$. The current slip rate on i^{th} slip system is a function of current τ_{ext}^i and g^i (Eqs. (11a and b), main text), and therefore, its Taylor expansion is

$$\dot{\gamma}_{t+\ddot{A}t}^i = \dot{\gamma}_t^i + \frac{\partial\dot{\gamma}^i}{\partial\tau_{ext}^i}\ddot{A}\tau_{ext}^i + \frac{\partial\dot{\gamma}^i}{\partial g^i}\ddot{A}g^i \tag{S3}$$

where $\Delta\tau_{ext}^i$ and Δg^i are the corresponding increments at Δt. From Eqs. (S1-S3), the incremental slip is

$$\ddot{A}\gamma^i = \ddot{A}t\left[\dot{\gamma}_t^i + \zeta\frac{\partial\dot{\gamma}^i}{\partial\tau_{ext}^i}\ddot{A}\tau_{ext}^i + \zeta\frac{\partial\dot{\gamma}^i}{\partial g^i}\ddot{A}g^i\right] \tag{S4}$$

Where $\ddot{A}g^i = \sum_j h_{ij}\ddot{A}\gamma^j$ (Eq. 11b, main text). The incremental RSS $\Delta\tau^i$ is

$$\ddot{A}\tau_{ext}^i = \left[C_{pqrs}\mu_{rs}^i + \omega_{pr}^i\sigma_{qr} + \omega_{qr}^i\sigma_{pr}\right]\left[\ddot{A}\varepsilon_{pq} - \sum_j \mu_{pq}^j\ddot{A}\gamma^j\right] \tag{S5}$$

where C_{pqrs} are the elastic moduli components, μ_{pq}^i and ω_{pq}^i are respectively the symmetric and skew-symmetric parts of the Schmid tensor, and σ_{pq} and $\Delta\varepsilon_{pq}$ are the macroscopic stress and incremental strain components. By combining these equations, we obtain

$$\begin{aligned}&\sum_j\left\{\delta_{ij} + \zeta\ddot{A}t\frac{\partial\dot{\gamma}^i}{\partial\tau_{ext}^i}\left[C_{pqrs}\mu_{rs}^i + \omega_{pr}^i\sigma_{qr} + \omega_{qr}^i\sigma_{pr}\right]\mu_{mn}^i - \zeta\ddot{A}t\frac{\partial\dot{\gamma}^i}{\partial g^i}h_{ij}\mathrm{sign}\left(\dot{\gamma}_t^j\right)\right\}\ddot{A}\gamma^j \\ &= \dot{\gamma}_t^i\ddot{A}t + \zeta\ddot{A}t\frac{\partial\dot{\gamma}^i}{\partial\tau_{ext}^i}\left[C_{pqrs}\mu_{rs}^i + \omega_{pr}^i\sigma_{qr} + \omega_{qr}^i\sigma_{pr}\right]\ddot{A}\varepsilon_{pq}\end{aligned} \tag{S6}$$

where, within a TBAZ

$$\frac{\partial \dot{\gamma}^{i}}{\partial \tau_{ext}^{i}} = \frac{\partial_{z}\dot{\gamma}^{i}}{\partial \tau_{ext}^{i}} = m_z \dot{\gamma}_0 \frac{1}{\tau_0^i}\left|\frac{\tau_{ext}^{i}}{\tau_0^i}\right|^{m_z-1} + m_z \dot{\gamma}_0 \frac{1}{g^i}\left|\frac{\tau_{ext}^{i}}{g^i}\right|^{m_z-1} \quad \text{(S7)}$$

and,

$$\frac{\partial \dot{\gamma}^{i}}{\partial g^{i}} = \frac{\partial \dot{\gamma}_{dz}^{i}}{\partial g^{i}} = -m_z \dot{\gamma}_0 \frac{1}{g^i}\left|\frac{\tau_{ext}^{i}}{g^i}\right|^{m_z-1} \frac{\tau_{ext}^{i}}{g^i} \quad \text{(S8)}$$

In the parent region,

$$\frac{\partial \dot{\gamma}^{i}}{\partial \tau_{ext}^{i}} = \frac{\partial_{p}\dot{\gamma}^{i}}{\partial \tau_{ext}^{i}} = m_p \dot{\gamma}_0 \frac{1}{g^i}\left|\frac{\tau_{ext}^{i}}{g^i}\right|^{m_p-1} \quad \text{(S9)}$$

and,

$$\frac{\partial \dot{\gamma}^{i}}{\partial g^{i}} = \frac{\partial \dot{\gamma}_{dp}^{i}}{\partial g^{i}} = -m_p \dot{\gamma}_0 \frac{1}{g^i}\left|\frac{\tau_{ext}^{i}}{g^i}\right|^{m_p-1} \frac{\tau_{ext}^{i}}{g^i} \quad \text{(S10)}$$

Reference

[1] Needleman A, Asaro RJ, Lemonds J, Peirce D. Computer Methods in Applied Mechanics and Engineering 1985;52:689.